Numerical Analysis and Measurement of High In-Bore Magnetic Field of Synchronous Induction Coil Launcher

SHAOHUA GUAN [ID], **XIAOCUN GUAN** [ID], **JINGBIN SHI, AND BAOQI WU**
National Key Laboratory of Science and Technology on Vessel Integrated Power System, Naval University of Engineering, Wuhan 430033, China
Corresponding author: Xiaocun Guan (guanxiaocun2012@163.com)

ABSTRACT The high in-bore magnetic field generated by synchronous induction coil launcher (SICL) was analyzed and measured. According to the current filament method, the magnetic induction intensity generated by the drive coils and each armature filament were calculated. The magnetic field distribution law of the synchronous induction coil launcher was obtained through magnetic field superposition principle. Based on the Biot-Savart law, the equation for calculating magnetic induction intensity of synchronous induction coil launcher was deduced, and the numerical calculation model of magnetic field distribution of synchronous induction coil launcher was established. The magnetic field distribution and numerical calculation model when the drive coils discharge with or without armature were carried out, and the numerical calculation results of the magnetic induction intensity when the drive coils discharge were compared with the finite element simulation results. Finally, the accuracy of the numerical calculation model was verified by comparing the one-dimensional hall probe arranged on the single-stage test platform with the simulation results.

INDEX TERMS Numerical analysis, synchronous induction coil launcher (SICL), magnetic field, Biot-Savart law.

I. INTRODUCTION

Compared with the conventional chemical launch method, the synchronous induction coil launcher has the advantages of adjustable speed, high precision, long range and great power. It is mainly composed of drive coil and armature [1]–[4], which refers to that uses pulse current to generate magnetic traveling wave to drive the armature movement [5]–[7]. Fig.1 shows the structure of multi stage synchronous induction coil launcher, the armature is divided to n filaments by using current filament method [4]. It is suitable to accelerate the effective load with large mass to high speed which has important application prospects in the fields of air defense and missile defense, ultra-long-range suppression, and micro-satellite launch [8]–[10].

The integrated projectile for electromagnetic launch is mainly composed of projectile body and armature which pushes the projectile forward under the action of Lorentz force. Since the excitation current is generally up to kA level,

The associate editor coordinating the review of this manuscript and approving it for publication was Zhengqing Yun [ID].
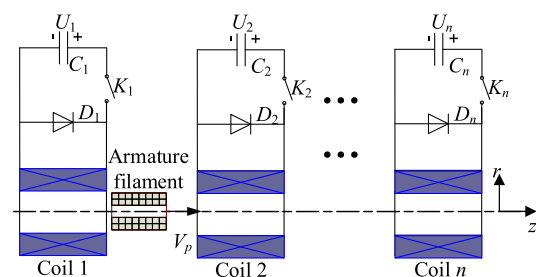

FIGURE 1. Structure of multi stage SICL.

the magnetic field in the launcher can reach more than a dozen Tesla, and the frequency is below several kHz. The low-frequency high magnetic field will cause the failure of the electronic components of the projectile and the occurrence of false signals that will bring some security problems. Therefore, it is necessary to analyze the distribution of the high in-bore magnetic field of synchronous induction coil launcher to provide guidance for the design of the integrated projectile for electromagnetic launch.

Without considering the influence of metal shell, the drive coil and armature can be regarded as hollow cylindrical

coil. The magnetic field distribution can be obtained by using the single integral method and the magnetic field superposition principle [11]. Lei Y. [11] gave the mathematical model of magnetic field of hollow cylindrical coil. Zhu Y. [12] also established the magnetic field calculation model according to Lei Y. [11], and used MATLAB software to analyze the magnetic field of synchronous induction coil launcher that obtained the distribution law of magnetic field. In Chen X. [13], a three-dimensional physical model whose spiral characteristics and asymmetry of the drive coil were fully considered of single-stage synchronous induction coil gun was established by finite element method. Wang X. [14] analyzed the relationship between the electromagnetic force and the axial gradient of the magnetic field, and proposed the method of installing magnetic conducting shell outside the drive coil to improve the magnetic field configuration. Zhao K. [15] established the mathematical model of eddy current field in the conductor region based on the combination of vector magnetic potential and scalar potential.

The above references analyzed the magnetic field distribution of synchronous induction coil launcher, but Zhu Y. [12] only considered the case of single-stage drive coil discharge, and not considered the coupling of multi-stage drive coils. The distribution of magnetic field is analyzed inside the drive coil through finite element simulation, but the mathematical model is not verified in [13]–[15]. Based on the structure model of the SICL, a three dimensional electromagnetic field numerical simulation model of it is established in this paper. The magnetic field distribution and the magnetic induction intensity of the fixed measuring point when the drive coil discharges with and without armature are compared, which provides the basis for the layout of the electronic components of the integrated projectile.

II. MATHEMATICAL MODEL OF MAGNETIC FIELD DISTRIBUTION

The following assumptions are made to establish the mathematical calculation model of magnetic field distribution of synchronous induction coil launcher,

(1) The axis center of the armature coincides with the axis center of the drive coil.

(2) The deformation of armature under the action of electromagnetic force are neglected.

(3) Each armature filament can be regarded as a single-turn coil [4].

According to the above assumptions, $\boldsymbol{B}$, $\boldsymbol{B}_{1b}$ and $\boldsymbol{B}_{2b} \ldots \boldsymbol{B}_{ib} \ldots \boldsymbol{B}_{Nb}$ are respectively the magnetic induction intensity generated by the drive coil and the i-th $(i = 1 \ldots N)$ armature filament [16]–[18].

The magnetic field $\boldsymbol{B}_z = \boldsymbol{B} + \boldsymbol{B}_{1b} + \boldsymbol{B}_{2b} + \ldots + \boldsymbol{B}_{ib} + \ldots + \boldsymbol{B}_{Nb}$ of the single-stage synchronous induction coil launcher can be obtained due to the magnetic field superposition principle. According to the model single-stage synchronous induction coil launcher in Fig.2, the $\boldsymbol{B}_z$ has two components: the radial component $\boldsymbol{B}_{zr}$ and the

axial component $\boldsymbol{B}_{zz}$.

$$\boldsymbol{B}_{zr} = \boldsymbol{B}_r + \boldsymbol{B}_{1br} + \boldsymbol{B}_{2br} + \ldots + \boldsymbol{B}_{ibr} + \ldots + \boldsymbol{B}_{Nbr} \quad (1)$$

$$\boldsymbol{B}_{zz} = \boldsymbol{B}_z + \boldsymbol{B}_{1bz} + \boldsymbol{B}_{2bz} + \ldots + \boldsymbol{B}_{ibz} + \ldots + \boldsymbol{B}_{Nbz} \quad (2)$$

Since the drive coil and each armature filament can be regarded as a cylindrical coil, this paper calculates the magnetic field distribution of the drive coil and armature by using the single integral method [19]–[22]. It can be seen from (1)-(2) that the magnetic induction intensity components of drive coil and each armature filament can be calculated to obtain the magnetic field distribution law of the synchronous induction coil launcher [23], [24].
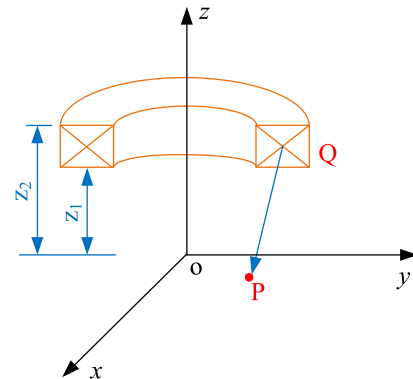

FIGURE 2. Magnetic field coordinates of SICL.

It is assumed that the inner and outer diameters of the drive coil respectively are $2R_1$ and $2R_2$, and the length is $2b$. As shown in Fig.2, the point P is set as arbitrary point inside the drive coil, the symmetric axis of the drive coil is set as the z axis, and the plane where point P located is set as the xoy plane. In the current distribution region V, the point $Q(r', \varphi', z')$ which the volume element is dV'. Assuming vector $\boldsymbol{QP} = \boldsymbol{r}$, according to the Biot-Savart law, we can obtain the magnetic field $\boldsymbol{B}$ [25],

$$\boldsymbol{B}(r, \varphi, z) = \frac{\mu_0}{4\pi} \int_V \frac{\boldsymbol{J} \times \boldsymbol{r}}{r^3} dV' = B_r \boldsymbol{e}_\rho + B_\varphi \boldsymbol{e}_\varphi + B_z \boldsymbol{e}_z \quad (3)$$

The three components of magnetic induction intensity of the point P are as following,

$$B_r = \frac{\mu_0 J}{2\pi} \int_0^\pi d\theta \int_{R_1}^{R_2} d\rho' \int_{z_1}^{z_2} \frac{-\rho' z' \cos \theta}{r^3} dz' \quad (4)$$

$$B_\varphi = 0 \quad (5)$$

$$B_z = \frac{\mu_0 J}{2\pi} \int_0^\pi d\theta \int_{R_1}^{R_2} d\rho' \int_{z_1}^{z_2} \frac{-\rho' (\rho' - \rho \cos \theta)}{r^3} dz' \quad (6)$$

where, μ_0 is the vacuum permeability

$$r = \sqrt{\rho'^2 + \rho^2 - 2\rho'\rho \cos \theta + z'^2}$$
$$\theta = \varphi' - \varphi$$

z_1 is the lower terminal axial coordinates of drive coil
z_2 is the upper terminal axial coordinates of drive coil

S. Guan *et al.*: Numerical Analysis and Measurement of High In-Bore Magnetic Field of Synchronous Induction Coil Launcher

IEEE *Access*

According to the relationship between current density and current of cylindrical coil,

$$J = \frac{NI}{2b(R_2 - R_1)} \quad (7)$$

Replace (4) with (1), (3) and (6) with (2), (3),

$$B_r = \frac{\mu_0 NI}{4b\pi(R_2 - R_1)} \int_0^\pi d\theta \int_{R_1}^{R_2} d\rho' \int_{z_1}^{z_2} \frac{-\rho' z' \cos\theta}{r^3} dz' \quad (8)$$

$$B_z = \frac{\mu_0 NI}{4b\pi(R_2 - R_1)} \int_0^\pi d\theta \int_{R_1}^{R_2} d\rho' \int_{z_1}^{z_2} \frac{-\rho'(\rho' - \rho\cos\theta)}{r^3} dz' \quad (9)$$

Taking the radial coordinates $\rho(\rho \neq 0)$ of point P as the reference value, each length value is reduced. Assuming $A_1 = R_1/\rho$, $A_2 = R_2/\rho$, $Z_1 = z_1/\rho$, $Z_2 = z_2/\rho$, $R = r/\rho$, $A = \rho'/\rho$, $Z = z'/\rho$, then the above equations are respectively transformed into following,

$$B_r = w \int_0^\pi d\theta \int_{A_1}^{A_2} dA \int_{Z_1}^{Z_2} \frac{-AZ\cos\theta}{R^3} dZ \quad (10)$$

$$B_z = w \int_0^\pi d\theta \int_{A_1}^{A_2} dA \int_{Z_1}^{Z_2} \frac{A(A - \cos\theta)}{R^3} dZ \quad (11)$$

where, $w = \frac{\mu_0 rNI}{4b\pi(R_2 - R_1)}$

$$R = \sqrt{1 + A^2 - 2A\cos\theta + Z^2}$$

The variables of the above two equations are integrated by using the repeated integral method,

$$B_r/w = \sum_{i,j=1}^2 (-1)^{i+j} F_r(A_i, Z_j) = F_r(A_1, Z_1)$$
$$- F_r(A_1, Z_2) - F_r(A_2, Z_1) + F_r(A_2, Z_2) \quad (12)$$

$$B_z/w = \sum_{i,j=1}^2 (-1)^{i+j} F_z(A_i, Z_j) = F_z(A_1, Z_1)$$
$$- F_z(A_1, Z_2) - F_z(A_2, Z_1) + F_z(A_2, Z_2) \quad (13)$$

The function $F_r(A, Z)$ is an even function about Z, and the function $F_z(A, Z)$ is an odd function about Z.

$$F_r(A, -Z) = F_r(A, Z); \quad F_z(A, -Z) = -F_z(A, Z)$$

The expression of function $F_r(A, Z)$ and $F_z(A, Z)$ respectively are as following,

$$F_r(A, Z) = \int_0^\pi [R + \cos\theta \, In(R + A - \cos\theta)] \cos\theta d\theta \quad (14)$$

$$F_z(A, Z) = \int_0^\pi \left\{ ZIn(R + A - \cos\theta) + \frac{\cos\theta}{2} In\left(\frac{R-Z}{R+Z}\right) \right.$$
$$\left. - \sin\theta \, arctg\left[\frac{Z(A - \cos\theta)}{R\sin\theta}\right] \right\} d\theta \quad (15)$$

The reduction of above equations cannot be used to calculate the magnetic field on the symmetric axis. When $r = 0$, there has only axial component of magnetic field, and the equations are as following,

$$B_z = \frac{\mu_0 NI}{4b(R_2 - R_1)} \left[(b - z) In\left(\frac{R_2 + \sqrt{R_2^2 + (b-z)^2}}{R_1 + \sqrt{R_1^2 + (b-z)^2}}\right) \right.$$
$$\left. + (b + z) In\left(\frac{R_2 + \sqrt{R_2^2 + (b+z)^2}}{R_1 + \sqrt{R_1^2 + (b+z)^2}}\right) \right] \quad (16)$$

$$B_r = 0 \quad (17)$$

The above equations are the simplest of the single integral equations currently which only has two quantities A and Z. Gaussian quadrature formula must be used in the calculation of magnetic field due to the above integral expression contains defects. According to the characteristics of the function F_r and F_z, using Gauss-Chebyshev quadrature formula is more convenient.

$$\int_{-1}^1 \frac{f(x)}{\sqrt{1-x^2}} dx = \frac{\pi}{n} \sum_{i=1}^n f\left(\cos\frac{2i-1}{2n}\pi\right) \quad -1 < \theta < 1 \quad (18)$$
$$+ \frac{\pi}{2^{2n-1}(2n)!} f^{2n}(\theta)$$

Let $x = \cos\theta$, then the equivalence equation of the above equation is as following.

$$\int_0^\pi f(\cos\theta) d\theta = \frac{\pi}{n} \sum_{i=1}^n f\left(\cos\frac{2i-1}{2n}\pi\right) + R_n \quad (19)$$

When the above equation is used to calculate F_r and F_z, the quadrature coefficient π/n and the quadrature point $\cos[(2i-1)\pi/2n]$ can be accurately calculated. Generally, $n \geq 15$ should be selected to achieve higher accuracy.

According to the above magnetic field calculation model, the magnetic field distribution under the action of single drive coil and armature filament can be obtained. For the multi-stage synchronous induction coil launcher, the magnetic field distribution is the superposition of magnetic field not only under the action of multiple drive coils but also under the action of armature filaments [26].

The above analysis about the magnetic field distribution of the synchronous induction coil launcher is under the ideal condition. In practice, the influence of the metal shell of the multi-stage synchronous induction coil launcher and the skin effect on the magnetic field distribution must be considered.

III. NUMERICAL AND SIMULATION ANALYSIS

Aimed at the numerical analysis about the magnetic field distribution of the synchronous induction coil launcher, the MATLAB numerical simulation and MAXWELL finite element simulation results are compared and analyzed in this section. The influence of metal shell on magnetic field distribution of the multi-stage synchronous induction coil
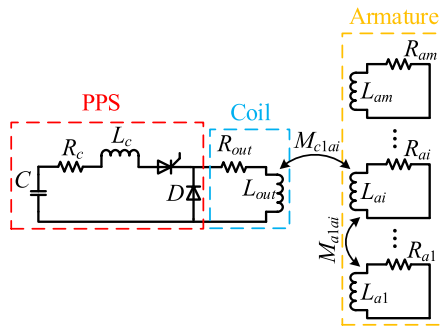
FIGURE 3. Equivalent circuit of single-stage SICL.

TABLE 1. Parameters for pulsed power supply and drive coil.

Component	Parameter	Value
PPS	resistance	15mΩ
	capacitance	16 mF
	voltage	3500V
Coil	length	102 mm
	outer diameter	68.5 mm
	inner diameter	33.5 mm
	turns	40
Armature	mass	6kg
	length	300mm
	outer diameter	29.5mm
	inner diameter	19.5mm
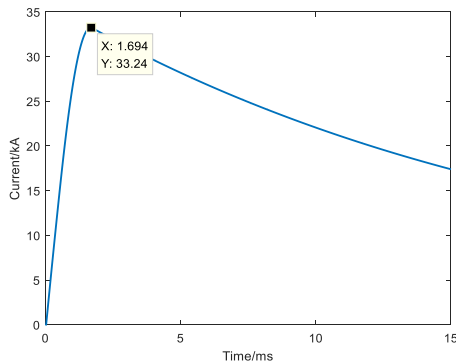
FIGURE 4. Current of drive coil.

launcher is not considered. The pulse power supply designed in the laboratory is the excitation current of the drive coil. The parameters of the capacitor bank and the drive coil are shown in Tab.1. The armature material is aluminium, and its initial position is that the tail of the armature is located at the center of the first-stage drive coil. The equivalent circuit of single-stage SICL is shown in Fig.3. R_c, R_{out} and $R_{ai}(i = 1, \ldots, m)$ represent the resistance of pulse power supply(PPS), coil and armature filament. L_c, L_{out} and $L_{ai}(i = 1, \ldots, m)$ represent the inductance of PPS, drive coil and armature filament. C represents the capacitance of PPS. D represents the diode. $M_{a1ai}(i = 1, \ldots, m)$ represents the mutual inductance of armature filaments, and $M_{c1ai}(i = 1, \ldots, m)$ represents the mutual inductance of drive coil and armature filament.
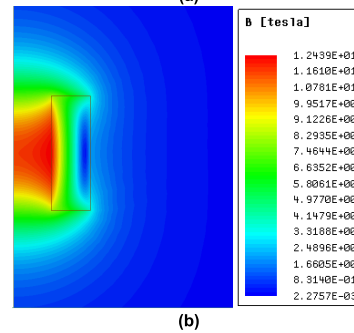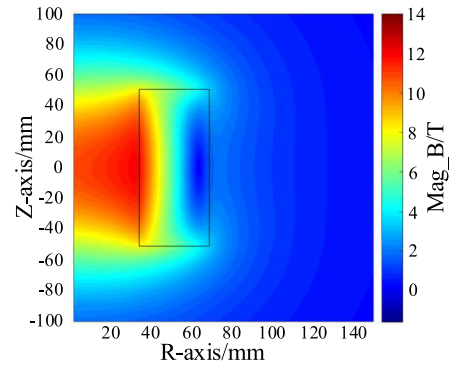

FIGURE 5. Total Magnetic field distribution of single stage drive coil without armature. (a) Numerical calculation results, (b) Simulation results.
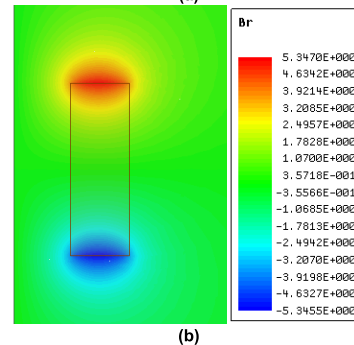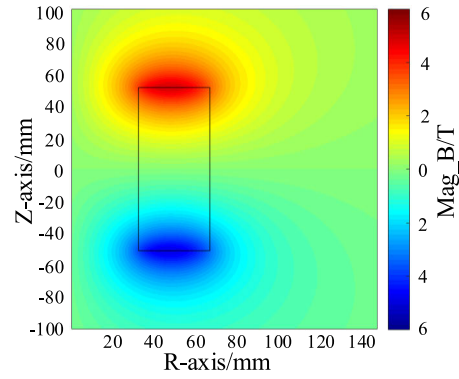

FIGURE 6. Radial magnetic field distribution of single stage drive coil without armature. (a) Numerical calculation results, (b) Simulation results.

A. MAGNETIC FIELD DISTRIBUTION WITHOUT ARMATURE
When the single-stage drive coil discharges without armature, the magnetic field distribution is completely symmetrical. The current of drive coil is shown in Fig.4 when the charging voltage is 3500 V. According to the Biot-Savart law, the larger
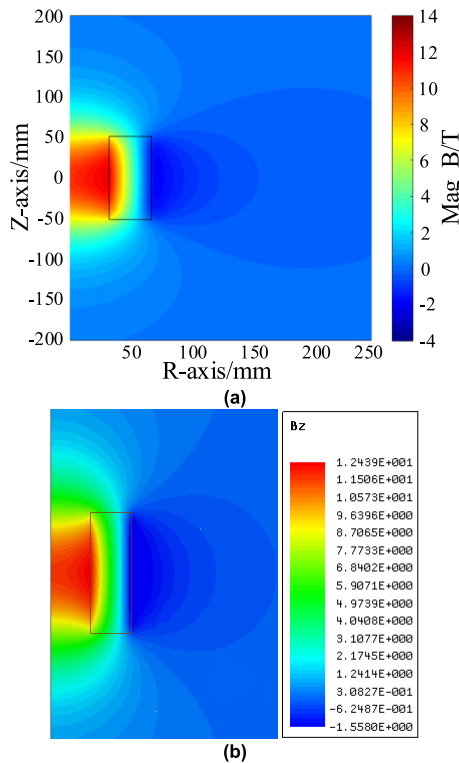
S. Guan *et al.*: Numerical Analysis and Measurement of High In-Bore Magnetic Field of Synchronous Induction Coil Launcher

IEEE *Access*

FIGURE 7. Radial magnetic field distribution of single stage drive coil without armature. (a) Numerical calculation results, (b) Simulation results.

the current amplitude is, the larger the current density is, and the larger the corresponding magnetic field at the same position is.

The magnetic field distribution at the peak current ($t = 1.694$ms, $I1 = 33.24$kA) is compared and analyzed. The drive coil and armature are symmetrical that the model can be simplified into two-dimensional structure.

Through the numerical calculation and finite element simulation, the distribution of the total magnetic field, the radial and axial magnetic fields are shown in Figs.5–7.

The drive coil is wrapped by Litz wire and its current density is evenly distributed. Therefore, it can be seen from Figs.5–7 that the total magnetic field and axial magnetic field generated by the single-stage drive coil without armature are symmetrically distributed about the radial direction of the drive coil center, and equal magnitude, same direction. The radial magnetic field is also symmetrically distributed, and although the magnitude is equal but the direction is opposite.

As shown in Fig.5, the magnetic field of inner region corresponding to the drive coil length can reach 12T. It can be seen from Fig.6 that the radial magnetic field generated by the drive coil is mainly distributed at both terminals of the drive coil, and the maximum amplitude is 5.3 T. Compared with the axial magnetic field in Fig.7, the magnetic field distribution law is basically the same as that of the total magnetic field. Therefore, the axial magnetic field generated by the drive coil is mainly the axial magnetic field which will generate radial force. So, the radial force is much larger than the axial force generated by the drive coil.
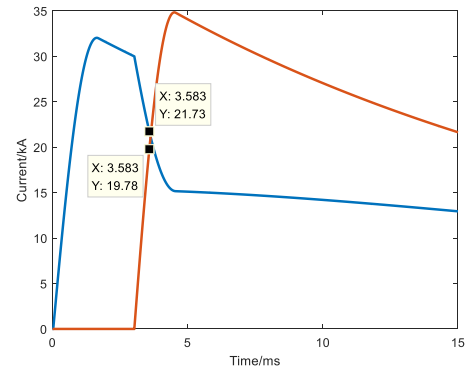

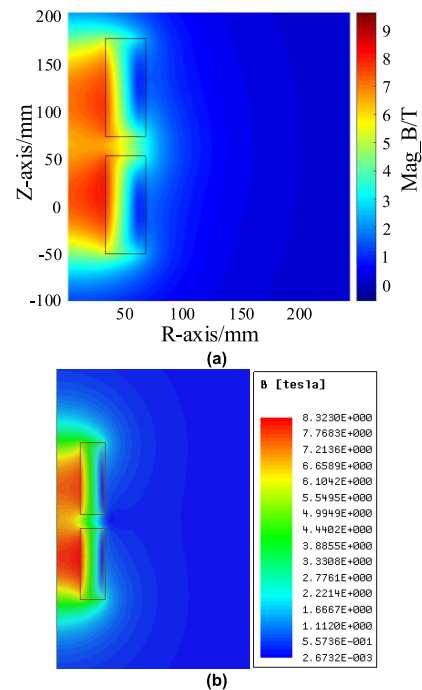**FIGURE 8.** Current of drive coil.

FIGURE 9. Total Magnetic field distribution of two stage drive coils without armature. (a) Numerical calculation results, (b) Simulation results.

When the two-stage drive coils discharge at different times, the current of it are different, and the magnetic field distribution is not completely symmetrical due to the superposition of magnetic field. When the charging voltage is 3500V, the current of the two-stage drive coils is shown in Fig.8. The discharge time interval between two drive coils is 3ms.

The magnetic field distribution of two-stage drive coils without armature is compared and analyzed.

When the current is 3.583ms($I1 = 21.73$kA, $I2 = 19.78$kA), the total, radial and axial magnetic field distribution are shown in Figs.9-11.

According to (3), the magnetic field is only proportional to the current density when the drive coil structure size is known. Therefore, the magnetic field generated by the two-stage drive coils is also approximately equal when the current of the two-stage drive coils is similar, and its distribution law is the same as that of the single-stage drive coil discharge without armature.
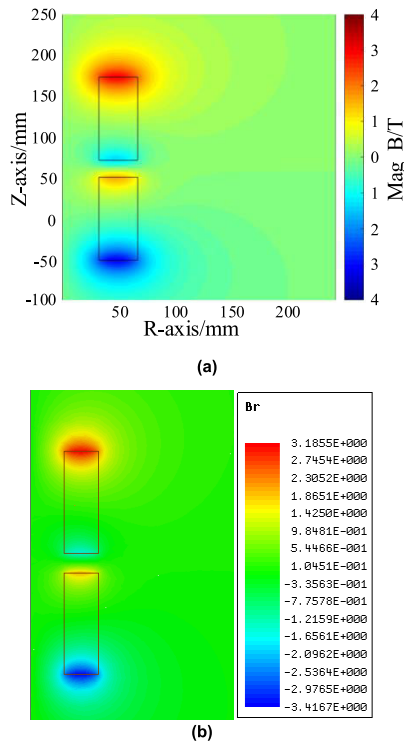
IEEE *Access*

S. Guan *et al.*: Numerical Analysis and Measurement of High In-Bore Magnetic Field of Synchronous Induction Coil Launcher

FIGURE 10. Total Magnetic field distribution of single stage drive coil without armature. (a) Numerical calculation results, (b) Simulation results.
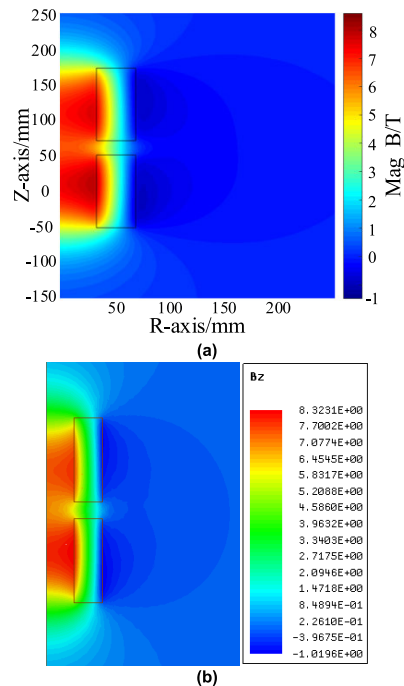

FIGURE 11. Axial Magnetic field distribution of two stage drive coils without armature. (a) Numerical calculation results, (b) Simulation results.

It can also be seen from Fig.9 that the maximum magnetic field in the first and second-stage drive coil respectively is 8.3 T and 7.7 T which is basically equal to the current amplitude ratio of the two-stage drive coils. Fig.10 is the same as Fig.6, but it can also be seen that the radial magnetic field generated by the drive coils at the adjacent terminal decreases
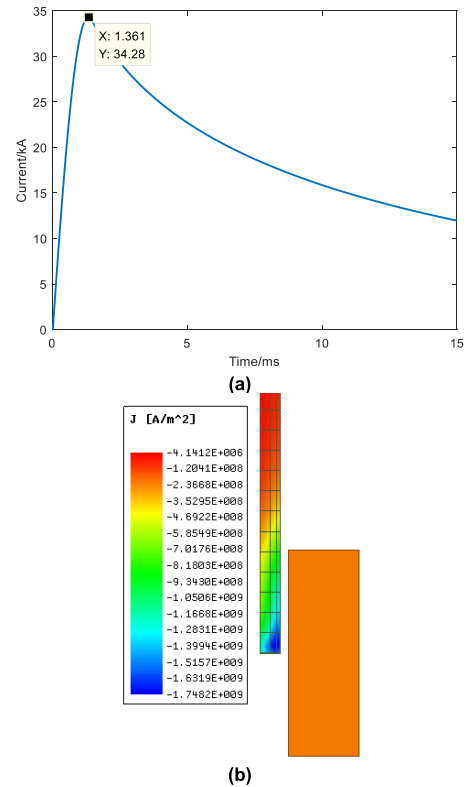

FIGURE 12. Current and current density distribution of single stage drive coil with armature. (a) Current of drive coil, (b) Current density distribution of armature.
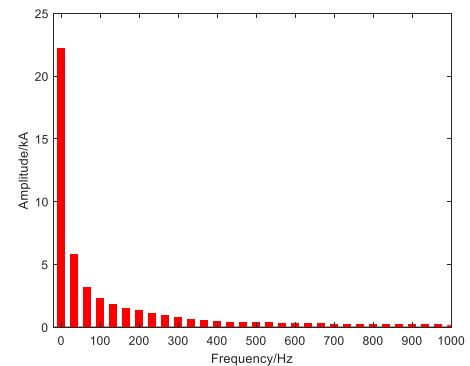

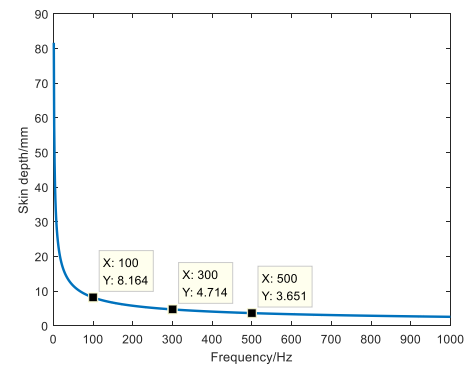**FIGURE 13.** Spectrum analysis of coil current.

FIGURE 14. Relationship between skin depth and frequency.

compared with the other terminal due to the opposite direction of magnetic field.

S. Guan *et al.*: Numerical Analysis and Measurement of High In-Bore Magnetic Field of Synchronous Induction Coil Launcher
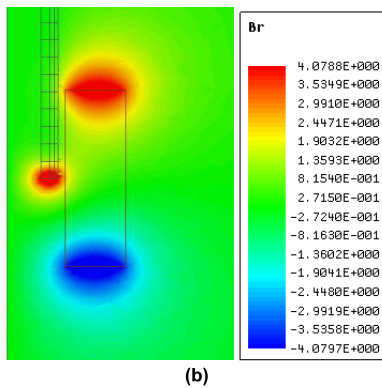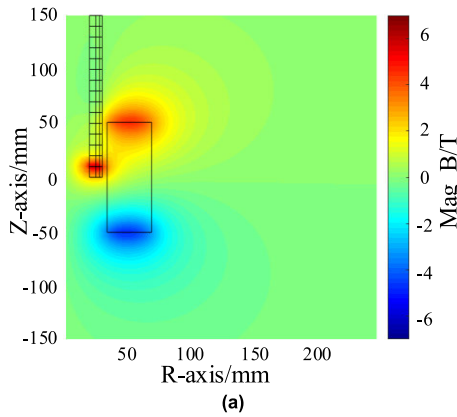
IEEE *Access*

FIGURE 15. Radial Magnetic field distribution of single stage drive coil with armature. (a) Numerical calculation results, (b) Simulation results.
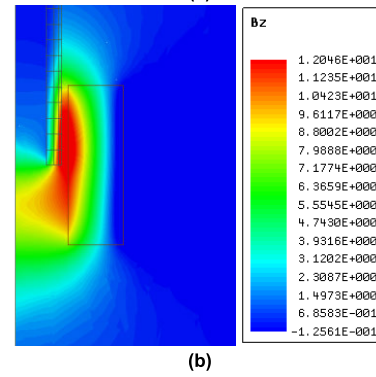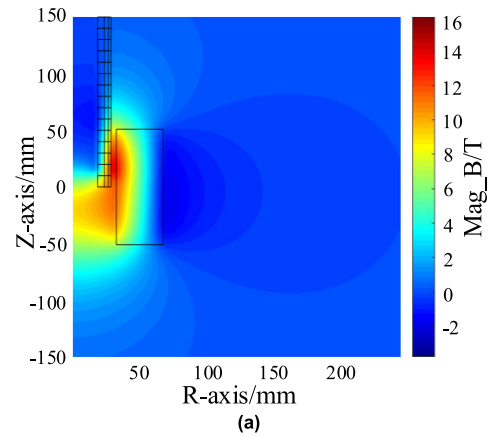

FIGURE 16. Axial Magnetic field distribution of single stage drive coil with armature. (a) Numerical calculation results, (b) Simulation results.

B. MAGNETIC FIELD DISTRIBUTION WITH ARMATURE

The initial position of the armature is in the center of the first stage drive coil and remains unchanged during the discharge of drive coil, so the existence of the armature makes the magnetic field distribution inside the single stage drive coil not symmetrical. The current of drive coil and the current density distribution of the armature are shown in Fig.12 when the charging voltage is 3500 V.

The spectrum analysis of coil current is carried out, and the amplitude corresponding to different frequencies is obtained as shown in the Fig.13. It can be seen that the frequency is mainly concentrated in the low frequency range. Usually, the depth of current penetrating into the conductor is called skin depth, which is represented by δ.

$$\delta = \sqrt{\frac{2}{\omega\sigma\mu}} \qquad (20)$$

where, ω is angular frequency (rad/s), $\omega = 2\pi f$, f is the frequency (Hz);

σ is the conductivity of the conductor material (S/m);

μ is the permeability of conductor material (H/m).

The relationship between the skin depth in the aluminium conductor and the frequency is shown in Fig.14. The electrical conductivity and relative permeability of aluminium is 3.5×10^7 S/m and 1 respectively. It can be seen that the skin depth decreases as the frequency increases.
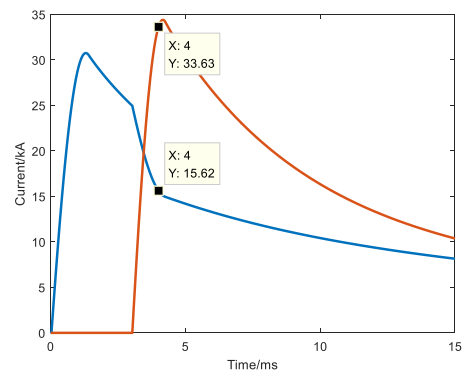

FIGURE 17. Current of drive coil.

According to the analysis, the armature is divided into axial and radial current filaments, the axial length is 10mm, and the radial thickness is 2mm, 3mm, and 5mm respectively in this paper and the induced current of each filament is evenly distributed. Fig.12 (b) shows that although the current density of each filament is not completely uniform, this paper assumes that the current density of each filament is still equivalent by the current density of the center of it.

The existence of armature makes the current of drive coil become larger and the time to reach the maximum is shortened. The magnetic field distribution at peak current (t = 1.361ms, I1 = 34.28kA) are compared. The radial and axial magnetic field distribution of numerical calculation and finite element simulation are shown in Figs.15-16.
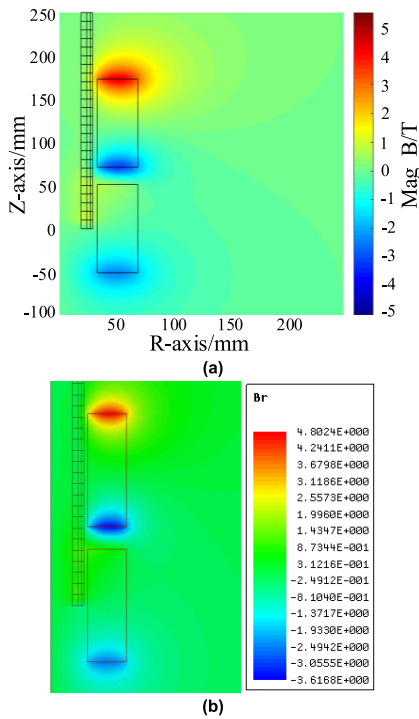
IEEE *Access*

S. Guan *et al.*: Numerical Analysis and Measurement of High In-Bore Magnetic Field of Synchronous Induction Coil Launcher

FIGURE 18. Radial Magnetic field distribution of two stage drive coils with armature. (a) Numerical calculation results, (b) Simulation results.
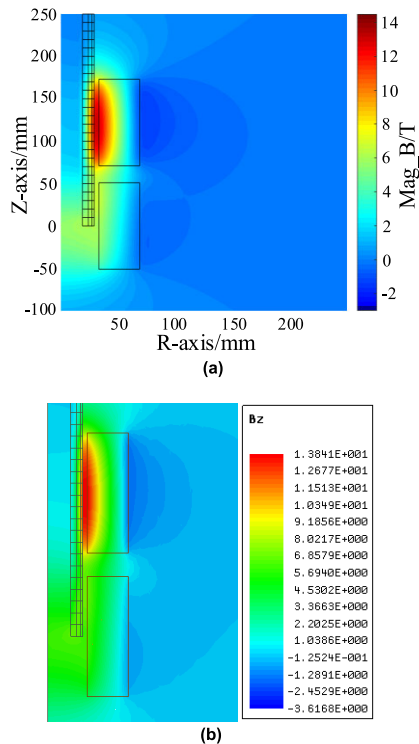

FIGURE 19. Axial Magnetic field distribution of two stage drive coils with armature. (a) Numerical calculation results, (b) Simulation results.

FIGURE 20. Magnetic induction intensity at different distances(a) Axial magnetic induction intensity, (b) Radial magnetic induction intensity.

FIGURE 21. Drive coil made of conductor with rectangle section. (a) Driving coil without helicity, (b) Section of rectangle conductor.

FIGURE 22. 3D model of drive coil.

As can be seen in Fig.15 and 16 that the radial and axial magnetic field of MATLAB numerical calculation are basically the same as the distribution law of MAXWELL finite element calculation when the single-stage drive coil dischar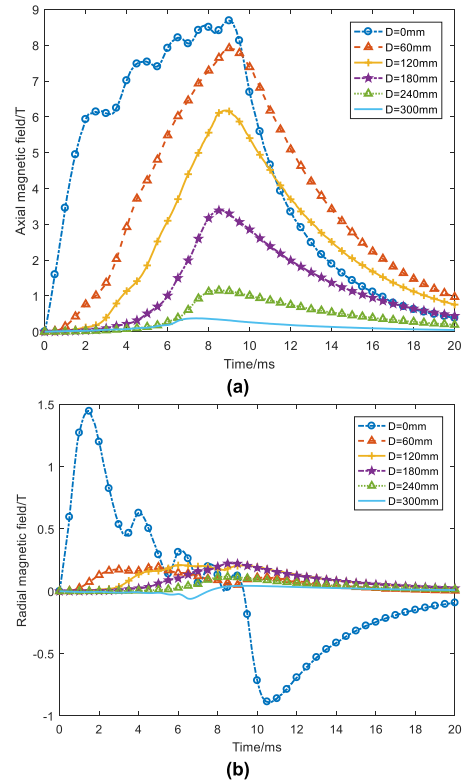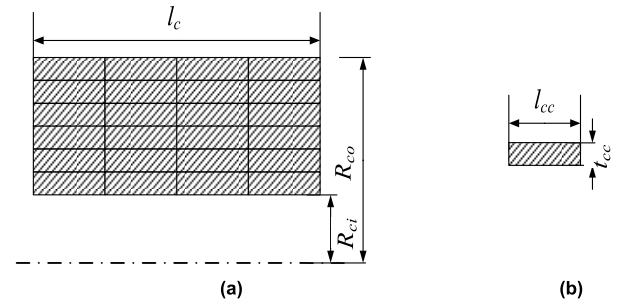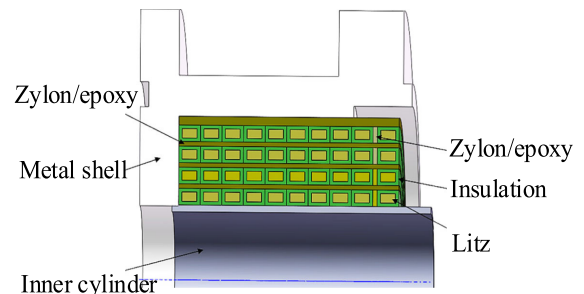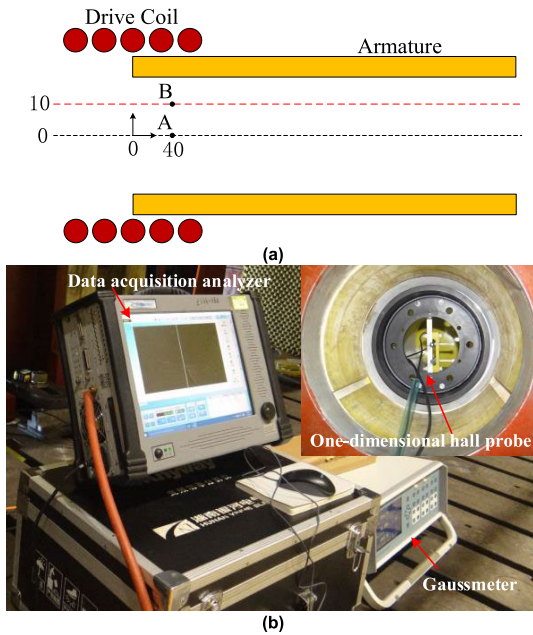ges with armature. It also can be seen that the magnetic field distribution on the armature is different. The main reason is that the current density of armature filament is equivalent by the current filament method and the skin effect cannot be considered, so there is an error in calculating the magnetic field generated by the induced current of armature filament.

S. Guan *et al.*: Numerical Analysis and Measurement of High In-Bore Magnetic Field of Synchronous Induction Coil Launcher

IEEE *Access*

FIGURE 23. Platform of magnetic field measurement. (a) Measurement point, (b) Measurement equipment.

The magnetic field distribution is also not symmetrical when the two-stage drive coils discharge at different times under the position of armature unchanged. The current of the two-stage drive coils is shown in Fig.17 when the charging voltage is 3500 V. The discharge time interval between two drive coils is also 3ms.

It can be seen from Fig.18 and 19 that the radial and axial magnetic field of MATLAB numerical calculation are basically the same as the distribution law of MAXWELL finite element calculation when the two-stage drive coils discharge with armature. Moreover, due to the current of the second-stage drive coil is 33.63 kA which is significantly higher than that of the first-stage drive coil of 15.62 kA, the magnetic induction intensity corresponding to the second-stage drive coil is significantly higher than that of the first-stage drive coil.

Fig.23(a) is a schematic diagram of the measuring point, the red virtual line as observation axis, and the distance D from the tail of armature is used as a reference. The magnetic induction intensity on the observation axis at different distances D is calculated. as shown in Fig.20.

It can be seen that with the increase of the distance from the armature tail, the magnetic induction intensity decreases obviously, and the time when the magnetic induction intensity reaches the maximum value is gradually advanced. When the distance D = 300mm, the maximum axial magnetic field is 0.37T, and the maximum radial magnetic field is 0.06T.

When the distance D = 0mm, the maximum axial magnetic field is 8.69T which is 23.5 times the maximum axial magnetic field of D = 300mm, the maximum radial magnetic field is 1.45T which is 24.2 times the maximum radial magnetic field of D = 300mm. Therefore, the electronic components can be arranged on the armature head and close to the center
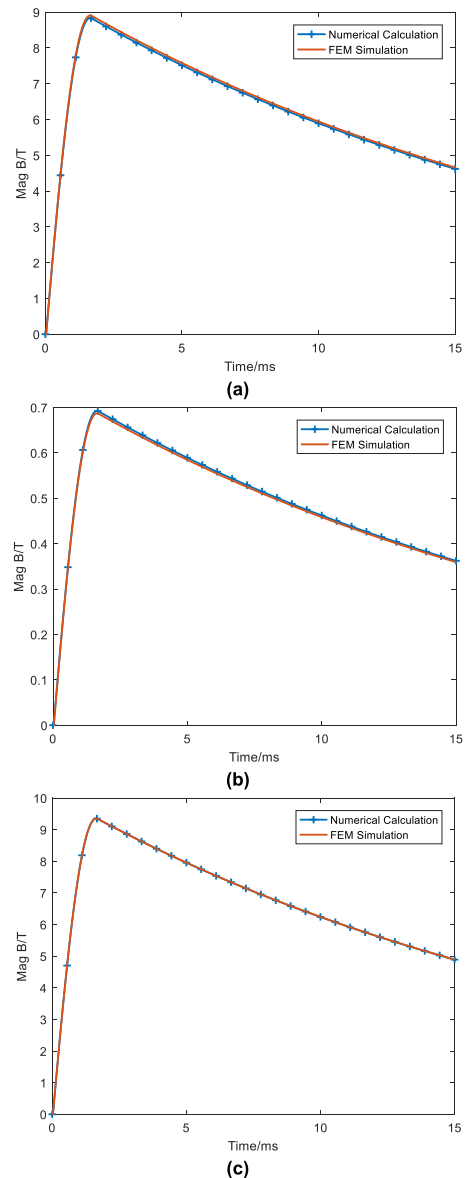
FIGURE 24. Magnetic induction intensity of single stage drive coil without armature. (a) Axial magnetic induction intensity of point A, (b) Radial magnetic induction intensity of point B, (c) Axial magnetic induction intensity of point B.

line in the subsequent electromagnetic design. The direction of the components can be arranged in the axial direction parallel to the axial magnetic field which can minimize the impact of the magnetic field on the electronic components.

IV. 3D ELECTROMAGNETIC FIELD SIMULATION AND EXPERIMENT

In this section, the magnetic field of the single-stage drive coil is measured to verify the correctness of the simulation results. Due to the actual equipment contains a metal shell which will affect the magnetic field for fixing the drive coil, so the finite element simulation can only be carried out by establishing a model with the same size as the equipment to obtain the magnetic field distribution.

IEEE *Access*

S. Guan *et al.*: Numerical Analysis and Measurement of High In-Bore Magnetic Field of Synchronous Induction Coil Launcher

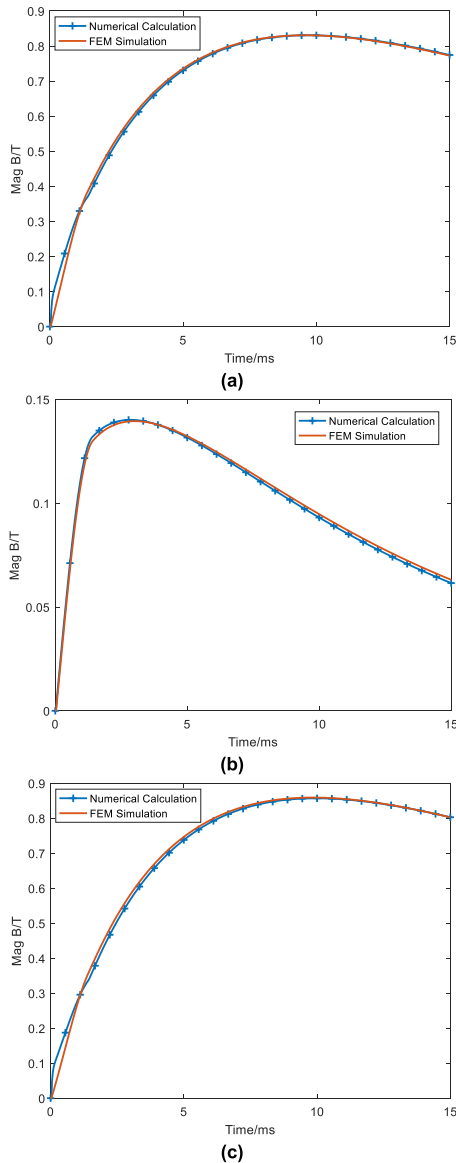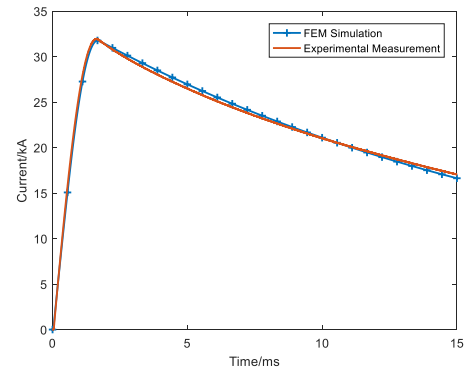
FIGURE 25. Magnetic induction intensity of single stage drive coil with armature. (a) Axial magnetic induction intensity of point A, (b) Radial magnetic induction intensity of point B, (c) Axial magnetic induction intensity of point B.

FIGURE 26. Comparison of drive coil current.

FIGURE 27. Comparison of axial magnetic induction intensity of point A of single stage drive coil without armature.

The induction coil is generally used for the measurement of time-varying magnetic field [15]. In Fig.23, the axial magnetic field when the drive coil discharges with and without armature at point A and B are measured by one-dimensional hall probe (one of the induction coils) and compared with the simulation results.

A. MAGNETIC FIELD OF SINGLE STAGE DRIVE COIL WITHOUT ARMATURE

The point A has only axial magnetic field when $r = 0$. Without considering the influence of shell, the numerical calculation and finite element method simulation (FEM simulation) results of magnetic induction intensity of point A and B are compared when the single stage drive coil discharge without armature in Fig.24.

B. MAGNETIC FIELD OF SINGLE STAGE DRIVE COIL WITH ARMATURE

Keep the armature position unchanged, the numerical calculation and finite element method simulation (FEM simulation) results of magnetic induction intensity of point A and B are compared when the single stage drive coil discharge with armature in Fig.25.

C. EXPERIMENTAL VERIFICATION

Fig.26 shows the comparison of current of drive coil between FEM simulation and experimental measurement when the charging voltage is 3500 V. It can be seen that

In this paper, the drive coil is made of rectangular section Litz wire. The half-section structure of the drive coil and the cross-section of the Litz wire is shown in Fig.21.
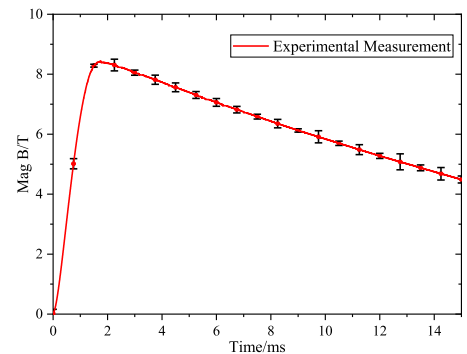
According to Fig.21, the turns N_c of the drive coil can be calculated which is equal to the turns N_1 of each layer multiplied by the number of layers N_2.

$$N_c = N_1 \cdot N_2 = \frac{l_c(R_{co} - R_{ci})}{l_{cc} \cdot t_{cc}} \tag{21}$$

As shown in Fig.22, The thickness of Zylon/epoxy is 2 mm which used to constrain the electromagnetic force and ensure the reliability of drive coil strength. The reinforced mica tape which the unilateral width is 0.5 mm can meet the insulation requirements of drive coil. Therefore, the Litz wire size is 9mm*6.25mm and the cross-sectional area is 56.25mm².

S. Guan *et al.*: Numerical Analysis and Measurement of High In-Bore Magnetic Field of Synchronous Induction Coil Launcher

IEEE *Access*

FIGURE 28. Comparison of axial magnetic induction intensity of point B of single stage drive coil without armature.
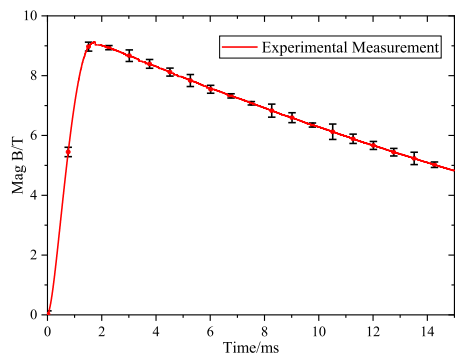

FIGURE 30. Comparison of axial magnetic induction intensity of point A of single stage drive coil with armature.

FIGURE 29. Comparison of drive coil current.

FIGURE 31. Comparison of axial magnetic induction intensity of point B of single stage drive coil with armature.
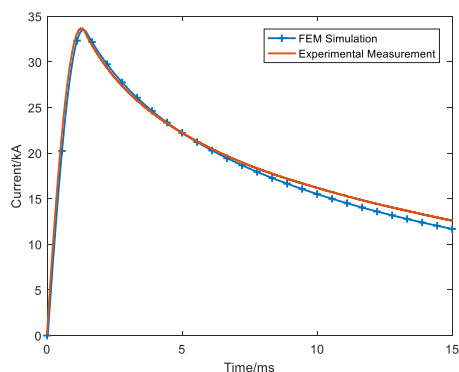
the experimental result is in good agreement with the FEM simulation. The peak current of experimental measurement is 31.96 kA and the peak current of simulation calculation is 31.87 kA which are respectively reduced by 1.28 kA and 1.37 kA compared with peak current in Fig.4. The main factor affecting the current reduction is that the shell will produce reverse eddy current when the drive coil discharge.

The coordinates of point A and B are (0mm, 0mm, 40mm) and (10mm, 0mm, 40mm). Multiple experiments were carried out and the standard deviation between experimental measurement and FEM simulation was calculated. Fig.27 and 28 respectively show the axial magnetic induction intensity of point A and B through the experimental curves with an error bar.

It can be seen from Fig.27 and 28 that the magnetic induction intensity is basically consistent with the drive coil current when it discharges without armature. The axial magnetic induction intensity of experimental measurement is in good agreement with simulation calculation, the standard deviation of each calculation point is small. The standard deviation of descending edge of magnetic induction intensity is relatively large. The reason is the magnetic induction intensity of experimental measurement is affected by the shell when the drive coil discharge.

Fig.29 shows the comparison of drive coil current between FEM simulation and experimental measurement under the charging voltage of 3500 V with armature. It can be seen that the experimental result is in good agreement with the
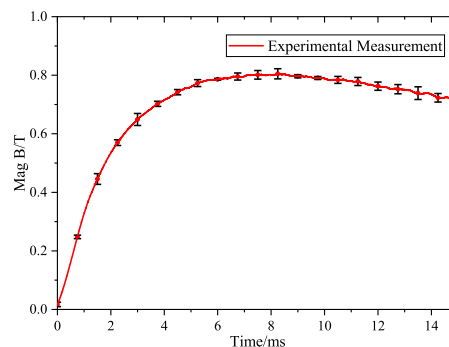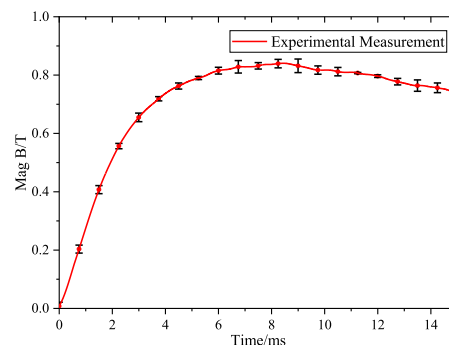
simulation results. The peak current of experimental measurement and simulation calculation respectively is 33.16 kA and 33.04 kA which is respectively reduced by 1.12 kA and 1.24 kA compared with peak current in Fig.12(a).

It can be seen from Fig.30 and 31 that the rise and fall rates of the magnetic induction intensity are relatively slow when the drive coil discharges with armature. The reason is that the armature generates reverse eddy current which will inhibit the increase of the magnetic induction intensity at the rising edge and slow down the decrease of it at the descending edge in the process of drive coil discharge. The standard deviation of each calculation point is also small, so the axial magnetic induction intensity of experimental measurement is also in good agreement FEM simulation.

V. CONCLUSION
During the launching of integrated projectile in electromagnetic launcher, the high in-bore magnetic field has great influence on the layout of electronic components inside the projectile. In this paper, the three-dimensional numerical model of magnetic field is established based on the superposition principle of magnetic field and Biot-Savart equation. The magnetic field distributions of single-stage and two-stage drive coil are analyzed by numerical and finite element method. The simulation results show that the magnetic induction intensity with armature is significantly smaller than that without armature, and the magnetic induction intensity decreases rapidly along the armature length direction. The numerical calculation is in good agreement with the finite

element simulation results. At the same time, the correctness of the model is verified by experiments, which has a certain guiding role for the layout of electronic components in the integrated projectile design.

REFERENCES

[1] X. Li, H. S. Wang, S. Z. Chen, and J. H. Liu, "Design and test of a five-section linear induction coil launcher," in *Proc. IEEE Int. Conf. Appl. Supercond. Electromagn. Devices (ASEMD)*, Nov. 2015, pp. 422–424.

[2] G. Xiao-Cun, L. Song-Cheng, L. Jun-Yong, and R. Zhou, "The launch performance analysis of the electromagnetic coil launcher continuous launch process with multiple armature," *IEEE Trans. Plasma Sci.*, vol. 45, no. 7, pp. 1519–1525, Jul. 2017.

[3] X. Niu, K. Liu, Y. Zhang, Z. Xiao, G. Xiao, and Y. Gong, "Research on self-consistent control strategy of multistage synchronous induction coil launcher," *Energy*, vol. 144, pp. 1–9, Feb. 2018.

[4] Z. Yadong, X. Gang, G. Yujia, N. Xiaobo, and L. Kaipei, "Armature structure research of a synchronous induction coil launcher," *IEEE Trans. Plasma Sci.*, vol. 45, no. 7, pp. 1574–1578, Jul. 2017.

[5] G. Fan, Y. Wang, K. Hou, Y. Miao, Y. Hu, and Z. Yan, "Research on energy conversion efficiency of the reconfigurable reconnection electromagnetic launcher," *Energy*, vol. 215, Jan. 2021, Art. no. 119088.

[6] T. Zhang, W. Guo, F. Lin, Z. Su, H. Zhang, Y. Chen, M. Li, and X. Sun, "Design and testing of 15-stage synchronous induction coilgun," *IEEE Trans. Plasma Sci.*, vol. 41, no. 5, pp. 1089–1093, May 2013.

[7] X. Niu, K. Liu, Y. Zhang, G. Xiao, and Y. Gong, "Multiobjective optimization of multistage synchronous induction coilgun based on NSGA-II," *IEEE Trans. Plasma Sci.*, vol. 45, no. 7, pp. 1622–1628, Jul. 2017.

[8] M. B. Perotoni, M. Mergl, and V. A. Bernaedes, "Coilgun velocity optimization with current switch circuit," *IEEE Trans. Plasma sci.*, vol. 45, no. 6, pp. 1015–1019, Jun. 2017.

[9] C. Qi, F. Han, S. Cui, and C. Yang, "Study on position detection method of multi-stage coilgun projectile," in *Proc. IEEE 8th Conf. Ind. Electron. Appl. (ICIEA)*, Jun. 2013, pp. 680–684.

[10] M.-G. Song, D.-V. Le, B.-S. Go, M. Park, and I.-K. Yu, "Design of a pulsed power system for using attractive force of multi-stage synchronous induction coilgun," in *Proc. IEEE 21st Int. Conf. Pulsed Power (PPC)*, Jun. 2017, pp. 1–4.

[11] L. Yinzhao, *Calculation of the Magnetic Field of Axisymmetric Coils*. Beijing, China: China Metrology Press, 1991.

[12] Z. Yanxia, W. Zhijun, and F. Junjian, "Numerical simulation analysis of magnetic field environment in electromagnetic track," *J. Ordnance Equip. Eng.*, vol. 38, no. 12, pp. 25–28, 2017.

[13] C. Xuehui, C. Yanjie, and W. Hengxue, "Research on 3D electromagnetic field model of synchronous induction coilgun," *J. Gun Launch Control*, vol. 2, pp. 13–17, Jun. 2013.

[14] W. Xiaozhao, Y. Cungui, and S. Zhaoming, "An optimization method of magnetic field configuration for electromagnetic coil launcher," *Ordnance Ind. Automat.*, vol. 37, no. 8, pp. 1–5, 2018.

[15] Z. Keyi, L. Zhiyuan, and C. Shukang, "Finite element analysis of magnetic field and eddy field in synchronous induction coil-gun," *High Voltage Eng.*, vol. 34, no. 3, pp. 492–495, 2008.

[16] W. Suwen, "Inductance tables of air-cored cylindrical coil," *J. Zhengzhou Univ. Eng. Sci.*, vol. 24, no. 3, pp. 106–112, Sep. 2003.

[17] F. Herlach, "Pulsed magnets for strong and ultra strong fields," *IEEE Trans. Magnetics*, vol. 32, no. 4, pp. 2438–2443, Jul. 1996.

[18] R. J. Kaye, E. L. Brawley, B. W. Duggin, E. C. Cnare, D. C. Rovang, and M. M. Widner, "Design and performance of a multi-stage cylindrical reconnection launcher," *IEEE Trans. Magn.*, vol. 27, no. 1, pp. 596–600, Jan. 1991.

[19] G. Fan, Y. Wang, K. Hou, Y. Miao, Y. Hu, and Z. Yan, "Research on energy conversion efficiency of the reconfigurable reconnection electromagnetic launcher," *Energy*, vol. 215, Jan. 2021, Art. no. 119088.

[20] X. Guan, J. Shi, S. Guan, and S. Wang, "Modeling and simulation of electromagnetic field of electromagnetic coil launcher," *IEEJ Trans. Electr. Electron. Eng.*, vol. 16, no. 4, pp. 635–643, Apr. 2021.

[21] X. Niu, J. Feng, W. Li, D. Jing, and Z. Zhang, "Effect of polarity reversal on performance of synchronous induction coil launcher," *IEEE Trans. Plasma Sci.*, vol. 48, no. 5, pp. 1343–1349, May 2020.

[22] B. Zhang, Y. Kou, K. Jin, and X. Zheng, "A multi-field coupling model for the magnetic-thermal-structural analysis in the electromagnetic rail launch," *J. Magn. Magn. Mater.*, vol. 519, Feb. 2021, Art. no. 167495.

[23] T. Zhang, W. Guo, Y. Liu, Z. Su, H. Zhang, W. Fan, and K. Huang, "Study on the characteristics of magnetic-field arrangement of synchronous induction coilgun," *IEEE Trans. Plasma Sci.*, vol. 48, no. 6, pp. 2316–2323, Jun. 2020.

[24] G. Becherini and B. Tellini, "Helicoidal electromagnetic field for coilgun armature stabilization," *IEEE Trans. Magn.*, vol. 39, no. 1, pp. 108–111, Jan. 2003.

[25] Z. Bengui, C. Yanjie, W. Jie, W. Huijin, and C. Xuehui, "Magnetic-structural coupling analysis of armature in induction coilgun," *IEEE Trans. Plasma Sci.*, vol. 39, no. 1, pp. 65–70, Jan. 2011.

[26] B.-S. Go, D.-V. Le, M.-G. Song, M. Park, and I.-K. Yu, "Design and electromagnetic analysis of an induction-type coilgun system with a pulse power module," *IEEE Trans. Plasma Sci.*, vol. 47, no. 1, pp. 971–976, Jan. 2019.

SHAOHUA GUAN received the B.S. degree in electrical engineering and its automation from Xi'an Jiaotong University, Xi'an, China, in 2014, and the M.S. degree from the Naval University of Engineering, Wuhan, China, in 2016. He is currently pursuing the Ph.D. degree with the National Key Laboratory of Science and Technology on Vessel Integrated Power System, Naval University of Engineering. His current research interest includes multiphasic numerical calculation of electrical devices.

XIAOCUN GUAN received the B.S. degree in mechanical design and manufacturing from the Hebei Institute of Agriculture, Baoding, China, in 2006, and the M.S. and Ph.D. degrees in mechanical and electrical engineering from the Shijiazhuang Mechanical Engineering College, Shijiazhuang, in 2009 and 2011, respectively. He is currently a Professor with the Naval University of Engineering, Wuhan, China. His research interests include coilgun, including the analysis of electromagnetic field, temperature field and stress field, and the design of prototypes.

JINGBIN SHI was born in Shanxi, China, in 1988. He received the B.S. and M.S. degrees in mechanical design and manufacturing and its automation from the Taiyuan University of Technology, Shanxi, China, in 2011 and 2014, respectively. He is currently pursuing the Ph.D. degree with the National Key Laboratory of Science and Technology on Vessel Integrated Power System, Naval University of Engineering. His current research interest includes electromagnetic launch technology.

BAOQI WU was born in Heilongjiang, China, in 1989. He received the B.S. and M.S. degrees from Harbin Engineering University, Harbin, China, in 2012 and 2015, respectively. He is currently pursuing the Ph.D. degree with the National Key Laboratory of Science and Technology on Vessel Integrated Power System, Naval University of Engineering. His current research interests include electromagnetic launch technology, system modeling, and simulation of coilgun.